

# Robust Tracking Control of Spherical Motion Platform for Virtual Reality

Seong-Min Lee , *Student Member, IEEE*, Kewei Xia , and Hungsun Son , *Member, IEEE*

**Abstract**—This article presents to develop a robust control system of spherical motion platform (SMP) capable of controlling six-degree-of-freedom motion, particularly unlimited rotational motion for better virtual reality. The SMP is the new design of a motion manipulator/simulator driven by the frictional force between a set of spherical wheels and cockpit sphere. However, it has intrinsic difficulties in control due to numerous uncertainties, including slipping motion between spherical wheels and cockpit sphere. Inaccurate motion control may degrade human perception as well as tracking performance. In this article, sliding mode control based on a disturbance observer is developed for the SMP to achieve precise motion tracking performance and provide a more realistic environment regardless of kinematic and dynamic uncertainties. Numerical simulation and experimental results with proportional–integral–differential and the robust controllers are compared for step and sinusoidal inputs to demonstrate the feasibility of motion control and tracking performance in spite of uncertainties. Finally, the SMP is operated using two representative flight maneuvers as a flight simulator. The results show that the SMP with the control system can be utilized to provide motion cue for a human on board for virtual reality.

**Index Terms**—Flight simulator, kinematic and dynamic uncertainties, robust tracking control, spherical motion platform (SMP).

## I. INTRODUCTION

MOTION simulators capable of multi-degree-of-freedom (DOF) motion have been widely developed for several decades to provide vivid motion realizing the virtual operational environments in the virtual reality (VR) area. Various motion simulators have been explored for motorcycle riding simulator [1], [2], vehicles [3]–[5], and flight simulators [6]–[9]. Most motion simulators are driven from two representative mechanisms: serial [4], [10] and parallel [1], [2], [11], [12] mechanisms. The

serial motion platform generally provides large workspaces but requires corresponding large operational space and actuator load for motion stiffness. Unlike the serial, motion simulators connected from the cockpit to base in parallel have been developed to improve rigidity. However, the geometries are still complex, having smaller workspace than serial simulators.

The motion range and limit can affect the performance such that the operator feels VR. The limited range of motion restricts continuous angular motion as well as angular velocity. Motion simulators driven by cable in parallel [8] with rotational workspaces  $\pm 40^\circ$  for roll, pitch, and  $\pm 5^\circ$  for yaw, and combined with serial and parallel mechanisms [5] with rotational workspaces  $\pm 15^\circ$  for roll, pitch, and yaw have been developed to enlarge translational range but needs huge space for the driving simulator. Unlike the parallel and serial motion platforms, the spherical actuators [13], [14] with a ball joint have been developed for an unlimited range of rotation but still limited tilting angle except for yaw motion. Atlas in [15] offers unlimited rotation motion, but another parallel mechanism is utilized for translation. Thus, a spherical motion platform (SMP) [16], [17], with a spherical cockpit, has been developed in contrast with existing motion simulators. The SMP provides smooth translation as well as rotation due to spherical wheels distinct from Atlas [15] based on Omni wheels. Despite the novel design, the SMP [16] still has kinematic and dynamic uncertainties, such as an imperfection of the large cockpit sphere, slipping between spheres and wheels, coupling effect between rotation and translation, and uncertain mass and inertia.

The performance of tracking control for simulators is crucial since the human inside cockpit can feel undesired motion and motion sickness due to delay between input command and output. Existing control systems based on an open-loop control for the SMP [16] cannot deal with uncertainties that degrade tracking performance and then cause a lack of motion cue for the human on board. A proportional–integral–differential (PID) control has been applied to rotate the cockpit sphere [18] but cannot guarantee the finite-time convergence and robustness of uncertainties. There are a number of controllers applied for controlling multi-DOF motion similar to the SMP. A sliding mode control (SMC) has been implemented to three DOFs orientation of the spherical actuator [14] to reject the dynamic uncertainties in finite time. Moreover, disturbance observer (DOB) based control [19] has been developed to estimate and compensate for the matched uncertainties, such as dynamic uncertainties. Similarly, a finite-time  $H_\infty$  control using the backstepping method [20] is designed to improve tracking performance for serial

Manuscript received November 30, 2019; revised February 25, 2020 and April 13, 2020; accepted April 14, 2020. Date of publication May 7, 2020; date of current version October 19, 2020. This work was supported in part by Future Innovation Research Funds (1.200034.01) of the Ulsan National Institute of Science and Technology, and in part by the Development of Multi-Degrees of Freedom Spherical Motion Platform (2.200020.01) of Civil Military Technology Cooperation Center. (Corresponding author: Hungsun Son.)

The authors are with the School of Mechanical, Aerospace, and Nuclear Engineering, Ulsan National Institute of Science and Technology, Ulsan 44919, South Korea (e-mail: leesm128@unist.ac.kr; kwxia134@gmail.com; hson@unist.ac.kr).

Color versions of one or more of the figures in this article are available online at <https://ieeexplore.ieee.org>.

Digital Object Identifier 10.1109/TIE.2020.2992001

manipulators under matched disturbances. Finite-time tracking control was also achieved from [11] and [21] for the Stewart motion platform despite uncertain dynamic models. Fuzzy control strategy has also been proposed for the spherical mobile platform [22] within unknown or uncertain dynamics. However, these controllers may have difficulties in attenuating mismatched uncertainties, including kinematic uncertainties such as distorted cockpit sphere, slipping, and coupled rotational motion. An alternative solution [23] for mismatched uncertainties has been designed but the tracking performance is still limited due to external disturbances. Thus, this article developed a robust control system to achieve trajectory tracking of the SMP in the presence of various uncertainties. The disturbance observer-based sliding mode control (DOB-SMC) is developed to estimate and compensate for kinematic and dynamic uncertainties. The tracking error is eventually converged in finite time.

The remainder of the article is organized as follows.

- 1) First, the kinematic and dynamic models of the SMP, including uncertainties, are analyzed for the robust control system. The kinematic model includes uncertainties of distorted cockpit sphere, slipping, surface contact, and coupled rotation due to translation. The dynamic uncertainties account for unknown inertia, gravity, friction, etc. The robust control system is introduced to cope with the unpredictable uncertainties.
- 2) The control strategy is proposed for tracking control of the cockpit regardless of uncertainties in a robust way. It proposed a DOB to estimate kinematic uncertainties and achieve finite-time convergence. Then, the DOB-SMC is designed to handle dynamic as well as kinematic uncertainties. The tracking error with the DOB-SMC can be converged in finite time by sliding motion along a designed sliding surface even in the presence of uncertainties.
- 3) The feasibility of the SMP motion control is validated from numerical simulations and experiments with a conventional PID and DOB-SMC. Motion control with the prototyped SMP is experimentally demonstrated. Moreover, the results show finite-time convergence in tracking performance. Two representative flight maneuvers, phugoid and dutch roll modes, are demonstrated. The results show capability and control performance as a flight simulator.

## II. MATHEMATICAL MODEL OF SMP

Fig. 1 shows a conceptual design of the SMP capable of controlling six DOFs motion of the cockpit sphere: three DOFs unlimited rotation and three DOFs translation. The rotation and translation of the cockpit are driven from the spinning of small spheres and movement of linear stages driven by ball screw actuators, respectively. The spherical wheel is composed of a small sphere, an active wheel driven by an actuator, and three passive rollers. The small sphere in the spherical wheel rotates along two axes, where one is driven by the actuator and free-rolling perpendicular to each other. Free-rolling motion can help the cockpit sphere to rotate smoothly without applying

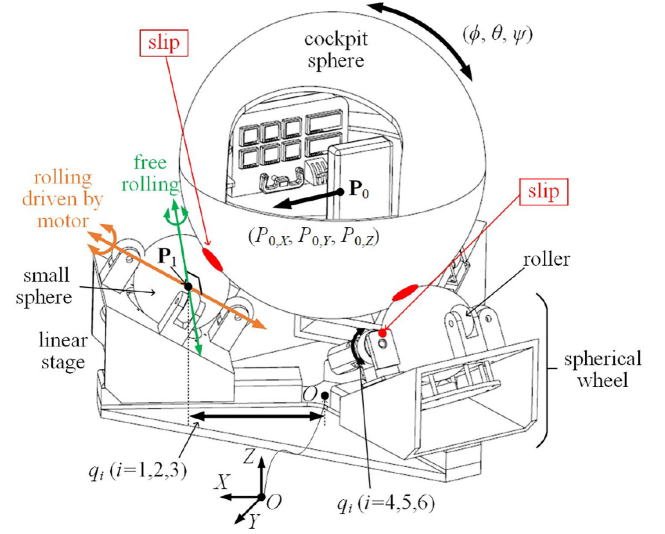


Fig. 1. Motion platform based on the spherical wheel [16].

brakes. However, the driving mechanism based on the frictional force has intrinsic difficulties in control due to slipping motion. It is necessary to understand the kinematic and dynamic models, including various uncertainties in order to design a robust control system. The kinematic equations are computed by using geometry between the cockpit and spherical wheels.

### A. Kinematics

The kinematic equations of the SMP can be derived by a rotation of the driving wheels and a relative position of linear stages [16]. The state vector  $\mathbf{x} = [P_{0,x} \ P_{0,y} \ P_{0,z} \ \phi \ \theta \ \psi]^T$  of the cockpit is expressed with XYZ coordinates in an inertial frame at the base center in Fig. 1. It can be expressed in terms of driving actuators and uncertainties in (1).

$$\dot{\mathbf{x}} = \mathbf{J}(\mathbf{q})\dot{\mathbf{q}} + \Delta_K, \quad \mathbf{J}(\mathbf{q}) = \begin{bmatrix} \mathbf{M}(\mathbf{q}) & \mathbf{0}_{3 \times 3} \\ \mathbf{N}_T(\mathbf{q}) & \mathbf{N}_R(\mathbf{q}) \end{bmatrix} \quad (1)$$

$$\mathbf{M}(\mathbf{q}) = [\partial \mathbf{P}_0 / \partial q_1 \quad \partial \mathbf{P}_0 / \partial q_2 \quad \partial \mathbf{P}_0 / \partial q_3] \quad (1a)$$

$$\mathbf{N}_T(\mathbf{q}) = [\mathbf{T}] [\mathbf{H} \times] \mathbf{M}(\mathbf{q}) \quad (1b)$$

$$\mathbf{N}_R(\mathbf{q}) \begin{bmatrix} \dot{q}_4 \\ \dot{q}_5 \\ \dot{q}_6 \end{bmatrix} = [\mathbf{T}] \frac{r_w}{\sqrt{2}R} \times \sum_{i=1}^3 \left( \begin{bmatrix} C_{\alpha_i} \\ S_{\alpha_i} \\ 1 \end{bmatrix} - \left( \mathbf{P}_{i0} \cdot \begin{bmatrix} C_{\alpha_i} \\ S_{\alpha_i} \\ 1 \end{bmatrix} \right) \frac{\mathbf{P}_{i0}}{\|\mathbf{P}_{i0}\|^2} \right) \dot{q}_{i+3} \quad (1c)$$

where

$$\mathbf{P}_0 =$$

$$\begin{bmatrix} (q_2 + q_3)(q_1^2 - q_2q_3) / 2(q_1q_2 + q_2q_3 + q_3q_1) \\ \sqrt{3}(q_2 - q_3)(q_1^2 + q_2q_3 + 2q_1(q_2 + q_3)) / 6(q_1q_2 + q_2q_3 + q_3q_1) \\ h + \sqrt{(r_s + R)^2 - (P_{0,x} - q_1)^2 + P_{0,y}^2} \end{bmatrix}$$

and

$$[\mathbf{T}] = \begin{bmatrix} \sec_{\theta} C_{\psi} & \sec_{\theta} S_{\psi} & 0 \\ -S_{\psi} & C_{\psi} & 0 \\ \tan_{\theta} C_{\psi} & \tan_{\theta} S_{\psi} & 1 \end{bmatrix}.$$

Here  $\mathbf{q} = [q_1 \ q_2 \ \dots \ q_6]^T$  is the joint coordinates corresponding to the output of actuators measurable from the encoder of each actuator, as shown in Fig. 1.  $\mathbf{J}(\mathbf{q})$  represents a Jacobian matrix for rotational and translational motions.  $\mathbf{x}$  and  $\dot{\mathbf{x}}$  are measurable using an inertial sensor installed on the cockpit. In (1a),  $\mathbf{M}(\mathbf{q})$  is derived from the partial derivative of  $\mathbf{P}_0$ , the position of the cockpit with respect to  $q_1, q_2$ , and  $q_3$ . The coupled rotation  $\mathbf{N}_T(\mathbf{q})$  according to translation in (1b) can be computed from (1a) and  $[\mathbf{H}\times]$ , a skew-symmetric matrix composed of  $\mathbf{H} = \sum (R\mathbf{P}_{0i}/\|\mathbf{P}_{0i}\|)$ ,  $i = 1, 2, 3$ . The rotational motion, according to  $q_4, q_5$ , and  $q_6$  from the actuator, can be shown in (1c) [16].  $\Delta_K$  represents kinematic uncertainties, which can be mainly caused by two factors: one is slip motion of actuator wheels, small spheres, and cockpit sphere. The wheels and spheres made of urethane are worn down at the contact in Fig. 1. The contact between the wheels eventually becomes surface, not a point for the rolling motion, which causes slipping motion. The others are mechanical and geometrical imperfections caused by manufacturing error. In a real application, it is difficult to manufacture the cockpit as a perfect sphere. The asymmetric configurations ( $q_1 \neq q_2 \neq q_3$ ) can also incur uncertain geometric relations with high nonlinearity. These kinematic uncertainties can be estimated from the observer.

### B. Dynamics

Dynamic equations of motion for the cockpit sphere are derived by Lagrangian formulation in terms of Euler angles ( $\phi, \theta, \psi$ ) using ZYX coordinates transformation from the inertial to the body frame. It is necessary to represent the cockpit orientation using Euler angles since the range of most flight maneuver is  $-90^\circ \leq \phi, \theta \leq 90^\circ$ , and  $-180^\circ \leq \psi \leq 180^\circ$ . The dynamic equations of motion are given as follows:

$$\mathbf{M}_A \ddot{\mathbf{x}} + \mathbf{f}(\mathbf{x}, \dot{\mathbf{x}}) + \Delta_D = \mathbf{u} \quad (2)$$

$$\mathbf{M}_A = \begin{bmatrix} m\mathbf{I}_{3 \times 3} & \mathbf{0}_{3 \times 3} \\ \mathbf{0}_{3 \times 3} & \mathbf{I}_R \end{bmatrix}$$

$$\text{where } \mathbf{I}_R = \begin{bmatrix} I_a & 0 & -I_a S_{\theta} \\ 0 & I_t & 0 \\ -I_a S_{\theta} & 0 & I_a S_{\theta}^2 + I_t C_{\theta}^2 \end{bmatrix} \quad (2a)$$

$$\mathbf{f}(\mathbf{x}, \dot{\mathbf{x}}) = \begin{bmatrix} \mathbf{0}_{3 \times 1} \\ -I_a C_{\theta} \dot{\theta} \dot{\psi} \\ (I_t - I_a) S_{\theta} C_{\theta} \dot{\psi}^2 + I_a C_{\theta} \dot{\phi} \dot{\psi} \\ 2(I_a - I_t) S_{\theta} C_{\theta} \dot{\theta} \dot{\psi} - I_a C_{\theta} \dot{\phi} \dot{\theta} \end{bmatrix} \quad (2b)$$

where  $\mathbf{M}_A$  is inertia matrix and  $m$  is cockpit mass;  $\mathbf{u} \in \mathbb{R}^6$  includes control input forces and torques.  $I_a$  and  $I_t$  are axial and transverse moment of inertia, respectively;  $S$  and  $C$  indicate sine and cosine functions of the subscript angle, respectively. In (2b),  $\mathbf{f}(\mathbf{x}, \dot{\mathbf{x}})$  represents the Coriolis effect of the cockpit sphere. The

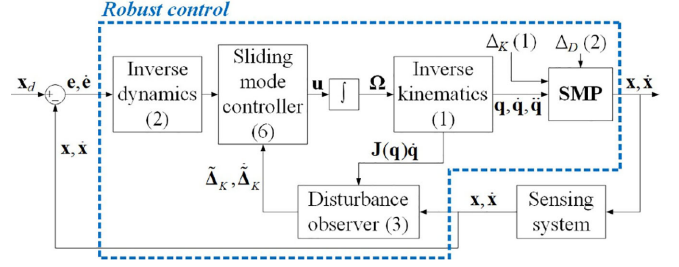


Fig. 2. Robust control system for SMP.

dynamic uncertainties  $\Delta_D$  are mainly caused by mechanical and electrical components as well as a human onboard. Although the cockpit is designed as an operator sits close to the center of the cockpit, the center of mass cannot be identified precisely, neither the moment of inertia. It is inevitable that the eccentricity from equipment and human inside the cockpit can cause uncertain gravitational force and torque. The undesired kinematic and dynamic uncertainties reduce tracking performance. Thus, the robust control system is designed to deal with the uncertainties.

### III. TRACKING CONTROL DESIGN

Fig. 2 shows a control system to improve the accuracy of the SMP control due to the uncertainties in (1) and (2). The robust control system is developed to converge the tracking error in finite time. First, the finite-time DOB is designed to estimate kinematic uncertainties  $\Delta_K$ . Then, DOB-SMC is applied to compensate  $\Delta_K$  as well as dynamic uncertainties  $\Delta_D$  in a robust way.

The control system is designed on the basis of the following assumption regarding the uncertainties as well as unexpected disturbances of the SMP.

*Assumption 1:* The kinematic and dynamic uncertainties are unknown but bounded for all situations. That is

$$\|\Delta_K\| \leq \beta_0 + \beta_1 \|\dot{\mathbf{q}}\| \leq b_K$$

$$\|\Delta_D\| \leq \beta_2 + \beta_3 \|\mathbf{q}\| + \beta_4 \|\dot{\mathbf{q}}\|^2 \leq b_D$$

where  $\beta_0, \beta_1, \beta_2, \beta_3$ , and  $\beta_4$  are arbitrary positive constants.  $b_K$  and  $b_D$  are known as positive constants and  $\Delta_K, \Delta_D \in \mathbb{R}^6$ . In the actual system,  $\Delta_K$  and  $\Delta_D$  will be bounded eventually since  $\|\mathbf{q}\|$  and  $\|\dot{\mathbf{q}}\|$  are also bounded from the actuator limit.

*Assumption 2:* The kinematic uncertainties  $\Delta_K$  are a twice differentiable function and have  $\mathbf{L} = [L_1, L_2, \dots, L_6]^T$  where  $L_i$  is a positive Lipschitz constant,  $i = 1, 2, \dots, 6$ .

#### A. DOB for Kinematic Uncertainties

A second-order sliding mode DOB is implemented to observe  $\hat{\Delta}_K$  as well as  $\dot{\hat{\Delta}}_K$  as follows [24]:

$$\begin{bmatrix} \dot{\mathbf{z}}_0 \\ \dot{\mathbf{z}}_1 \\ \dot{\mathbf{z}}_2 \end{bmatrix} = \begin{bmatrix} -\lambda_0 \mathbf{L}^{[1/3]} \langle \mathbf{z}_0 - \mathbf{x} \rangle^{2/3} + \mathbf{z}_1 + \mathbf{J}(\mathbf{q}) \dot{\mathbf{q}} \\ -\lambda_1 \mathbf{L}^{[1/2]} \langle \mathbf{z}_1 - \mathbf{v}_0 \rangle^{1/2} + \mathbf{z}_2 \\ -\lambda_2 \text{sgn}(\mathbf{z}_2 - \mathbf{v}_1) \end{bmatrix} \quad (3)$$

where  $v_0 = \dot{\mathbf{z}}_0 - \mathbf{J}(\mathbf{q})\dot{\mathbf{q}}$ ,  $v_1 = \dot{\mathbf{z}}_1$  and  $\hat{\mathbf{x}} = \mathbf{z}_0$ ,  $\hat{\Delta}_K = \mathbf{z}_1$ ,  $\hat{\Delta}_K = \mathbf{z}_2$ ;  $\lambda_0$ ,  $\lambda_1$ , and  $\lambda_2$  are positive constants;  $\hat{\mathbf{x}}$ ,  $\hat{\Delta}_K$ , and  $\hat{\Delta}_K$  are the estimates of  $\mathbf{x}$ ,  $\Delta_K$ , and  $\dot{\Delta}_K$ , respectively;  $\langle \mathbf{a} \rangle^p = [|a_1|^p \text{sgn}(a_1) |a_2|^p \text{sgn}(a_2) \cdots |a_l|^p \text{sgn}(a_l)]$  and  $\text{sgn}(\mathbf{a}) = [\text{sgn}(a_1) \text{sgn}(a_2) \cdots \text{sgn}(a_l)]^T$  for  $\mathbf{a} = [a_1 a_2 \cdots a_l]^T$ ;  $\mathbf{L}^{[n]} = \text{diag}(L_1^n, L_2^n, \dots, L_6^n)$ . Combining (1) and (3), the estimation errors for the observer can be obtained as follows:

$$\begin{aligned}\dot{\mathbf{e}}_0 &= -\lambda_0 \mathbf{L}^{[1/3]} \langle \mathbf{e}_0 \rangle^{2/3} + \mathbf{e}_1 \\ \dot{\mathbf{e}}_1 &= -\lambda_1 \mathbf{L}^{[1/2]} \langle \mathbf{e}_1 - \dot{\mathbf{e}}_0 \rangle^{1/2} + \mathbf{e}_2 \\ \dot{\mathbf{e}}_2 &\in -\lambda_2 \text{sgn}(\mathbf{e}_2 - \dot{\mathbf{e}}_1) + [-\mathbf{L}, \mathbf{L}]\end{aligned}\quad (4)$$

where  $\mathbf{e}_0 = \hat{\mathbf{x}} - \mathbf{x}$ ,  $\mathbf{e}_1 = \hat{\Delta}_K - \Delta_K$ ,  $\mathbf{e}_2 = \dot{\hat{\Delta}}_K - \dot{\Delta}_K$ .

Therefore, according to *Assumption 2* and [24], a finite-time stability of (4) can be ensured with chosen parameters  $\lambda_0$ ,  $\lambda_1$ , and  $\lambda_2$ , implying  $\hat{\mathbf{x}}$ ,  $\hat{\Delta}_K$ , and  $\dot{\hat{\Delta}}_K$  can be estimated from the observer in finite time  $T_0$ .

### B. Sliding Mode Controller Based on DOB Under Kinematic and Dynamic Uncertainties

An SMC system based on nonlinear dynamics is designed to handle the uncertain dynamics  $\Delta_D$  in (2) as well as kinematics  $\Delta_K$  to achieve that the cockpit sphere is driven to the desired position and orientation  $\mathbf{x}_d$  in finite time. First, the sliding surface is defined as

$$\sigma = \dot{\mathbf{e}} + c_1 \mathbf{e} + c_2 \int \mathbf{e} dt + \hat{\Delta}_K \quad (5)$$

where the tracking error is defined as  $\mathbf{e} = \mathbf{x}_d - \mathbf{x}$ ;  $c_1$  and  $c_2$  are positive constants. Then, the tracking control law  $\mathbf{u}$  can be designed as (6) using (3) and (5)

$$\mathbf{u} = \tau_A + k_1 \langle \sigma \rangle^p + \rho_D \text{sgn}(\sigma) \quad (6)$$

$$\begin{aligned}\tau_A &= \mathbf{f}(\mathbf{x}, \dot{\mathbf{x}}) + \mathbf{M}_A(\ddot{\mathbf{x}}_d + c_1(\dot{\mathbf{x}}_d - \mathbf{J}(\mathbf{q})\dot{\mathbf{q}} - \dot{\Delta}_K) \\ &\quad + c_2 \mathbf{e} + \dot{\hat{\Delta}}_K) + \frac{1}{2} \dot{\mathbf{M}}_A \sigma\end{aligned}\quad (6a)$$

where  $k_1$ ,  $\rho_D$ , and  $p$  are positive constants such that  $p < 1$ . The kinematics  $\mathbf{J}(\mathbf{q})\dot{\mathbf{q}}$  is computed from (1). The  $\dot{\hat{\Delta}}_K$  shown in (6a) can be observed from finite-time DOB in (3). The proposed control law can satisfy the following Theorem 1.

*Theorem 1:* The tracking errors of the cockpit sphere reach on the sliding surface  $\sigma$ , and sliding motion occurs with  $\sigma = \dot{\sigma} = 0$  within finite time  $T_1$

$$T_1 \leq \frac{\|\mathbf{M}_A\|^{(p+1)/2} V_1^{(1-p)/2}(0)}{k_1 \sqrt{2^{(1-p)}}(1-p)}. \quad (7)$$

*Proof:* The following equation can be obtained by differentiating (5) and applying (2) and (6):

$$\begin{aligned}\dot{\sigma} &= \ddot{\mathbf{x}}_d - \ddot{\mathbf{x}} + c_1(\dot{\mathbf{x}}_d - \mathbf{J}(\mathbf{q})\dot{\mathbf{q}} - \dot{\Delta}_K) + c_2 \mathbf{e} + \dot{\hat{\Delta}}_K \\ &= \ddot{\mathbf{x}}_d + c_1(\dot{\mathbf{x}}_d - \mathbf{J}(\mathbf{q})\dot{\mathbf{q}} - \dot{\Delta}_K) + c_2 \mathbf{e} + \dot{\hat{\Delta}}_K \\ &\quad - \mathbf{M}_A^{-1}(\mathbf{u} - \mathbf{f}(\mathbf{x}, \dot{\mathbf{x}}) - \Delta_D)\end{aligned}$$

$$= -\mathbf{M}_A^{-1} \left( \frac{1}{2} \dot{\mathbf{M}}_A \sigma + k_1 \langle \sigma \rangle^p + \rho_D \text{sgn}(\sigma) - \Delta_D \right) + c_1 \mathbf{e}_1. \quad (8)$$

Lyapunov candidate function is defined as  $V_1 = \frac{1}{2} \sigma^T \mathbf{M}_A \sigma$  to prove Theorem 1. The following equation can be computed from (8) and differentiating  $V_1$ . In (8),  $\dot{\mathbf{e}}$  is replaced with  $\mathbf{e}_1$  from observer shown in (4), and  $\sigma$  will not escape in finite time  $T_0$  [25], and finally,  $\mathbf{e}_1$  converges to zero after  $t > T_0$ .

$$\begin{aligned}\dot{V}_1 &= \frac{1}{2} \sigma^T \dot{\mathbf{M}}_A \sigma + \sigma^T \mathbf{M}_A \dot{\sigma} \\ &= \frac{1}{2} \sigma^T \dot{\mathbf{M}}_A \sigma - \sigma^T \left( \frac{1}{2} \dot{\mathbf{M}}_A \sigma + k_1 \langle \sigma \rangle^p + \rho_D \text{sgn}(\sigma) - \Delta_D \right) \\ &= -\sigma^T (k_1 \langle \sigma \rangle^p + \rho_D \text{sgn}(\sigma) - \Delta_D).\end{aligned}\quad (9)$$

The following equation can be computed from (8) and (9) applying *Assumption 1*:

$$\begin{aligned}\dot{V}_1 &\leq -\|\sigma\| (k_1 \|\sigma\|^p + \rho_D - b_D) \\ &\leq -k_1 \|\sigma\|^{p+1} \leq 0, \text{ for } \rho_D \geq b_D.\end{aligned}\quad (10)$$

Equation (9) can be expressed as the following equation by using  $2V_1(t) \leq \|\sigma\|^2 \|\mathbf{M}_A\|$  from the definition of Lyapunov candidate function  $V_1$ :

$$\begin{aligned}\dot{V}_1(t) &\leq -k_1 \left( \frac{1}{2} \|\sigma\|^2 \|\mathbf{M}_A\| \right)^{(p+1)/2} \frac{2^{(p+1)/2}}{\|\mathbf{M}_A\|^{(p+1)/2}} \\ &\leq -\alpha_1 V_1^{(p+1)/2}(t)\end{aligned}\quad (11)$$

where  $\alpha_1 = k_1 (2/\|\mathbf{M}_A\|)^{(p+1)/2} > 0$ . Finally, the following equation is computed from integration of (11), i.e.,  $\int V_1^{-(p+1)/2}(t) dV_1 \leq \int -\alpha_1 dt$ :

$$0 \leq V_1^{(1-p)/2}(t) \leq -\frac{1-p}{2} \alpha_1 t + V_1^{(1-p)/2}(0). \quad (12)$$

Eventually,  $V_1$  is bounded, and the sliding motion takes place with  $\sigma = \dot{\sigma} = 0$ . Therefore, it is validated that the closed-loop system is asymptotically stable, and the tracking error converges to 0 under kinematic and dynamic uncertainties after  $t > \max(T_0, T_1)$ .

## IV. NUMERICAL SIMULATION AND EXPERIMENT

The position and orientation tracking control of the SMP are demonstrated from numerical simulations with the comparison of PID, an integral sliding mode control (I-SMC), and the proposed DOB-SMC. The results of the estimation of kinematic uncertainties acquired from DOB are analyzed by comparison between simulations and experiments. Moreover, the tracking performance of the DOB-SMC is compared with the PID and I-SMC controller utilizing the prototyped SMP in experiments. For the experiment, the full cockpit sphere is manufactured using glass fiber reinforced plastic compared with the hemisphere [16] to satisfy the full rotational range along all axes, as shown in Fig. 3(a). Due to manufacturing defects, the cockpit sphere has slightly distorted top and bottom surfaces and becomes ellipsoid,



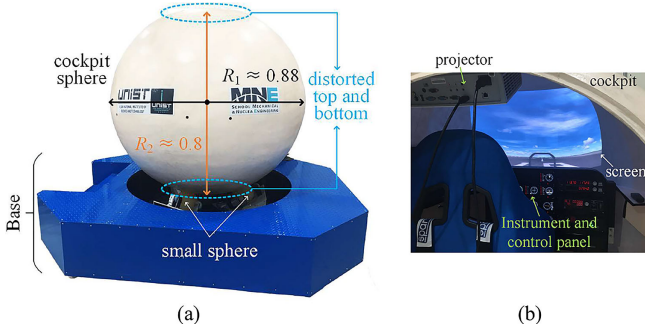


Fig. 3. Actual-scaled SMP with full cockpit sphere. (a) SMP. (b) Inside of the cockpit.

TABLE I  
LIST OF SPECIFICATIONS OF MECHANICAL PARAMETERS

$m$	150 kg	$I_a, I_t$	77.4 kg·m <sup>2</sup>
$r_w$	0.0375 m	$r_s$	0.11 m
$R$	0.88 m	$h_1$	0.35 m
$\gamma_1$	5 mm	$\gamma_2$	60
$q_{\text{forward limit}}$	0.285 m	$q_{\text{reverse limit}}$	0.745 m
$\dot{q}_{i,\text{sat}} (i=1,2,3)$	0.5 m/s	$\dot{q}_{i,\text{sat}} (i=4,5,6)$	600 °/s

TABLE II  
MOTION CAPABILITY FOR THE SMP

Rotational motion	$\phi$	$\theta$	$\psi$
Max. orientation (°)	±180	±90	±180
Max. angular velocity (°/s)	±32.3	±37.4	±57.6
Translational motion	$X$	$Y$	$Z$
Max. position (m)	±0.37	±0.43	±0.15
Max. linear velocity (m/s)	±0.5	±0.58	±0.57
Max. linear acceleration (m/s <sup>2</sup> )	±4.9	±5.7	±2.5

as shown in Fig. 3(a). In spite of kinematic and dynamic uncertainties caused by a manufacturing error, the DOB-SMC can accomplish the desired trajectory tracking of the cockpit sphere in the experiments. The mechanical parameters for orientation and position control are detailed in Table I. Table II presents the maximum workspace for the rotational and translational motion of the SMP from kinematics (1) with actuator limits in Table I.

The SMP requires six actuators to control both translation and rotational motion. The translational motion can be generated from three rotary actuators and ball screw actuators. The ball screw actuator has a lead  $\gamma_1$ , linear displacement according to the rotation of the ball screw. Three rotary actuators are utilized to rotate each small spheres for the rotational motion of the cockpit, and three gearboxes are installed in front of each actuator. The gear ratio of gearbox is  $\gamma_2$  given in Table I. According to the transmission of force and torque using the ball screw actuator and gearbox, respectively, the desired actuator velocity  $\dot{q}_a$  can be calculated from  $\dot{q}$  by using the following equation:

$$\dot{q}_a = \begin{bmatrix} (1/\gamma_1)I_{3 \times 3} & 0_{3 \times 3} \\ 0_{3 \times 3} & \gamma_2 I_{3 \times 3} \end{bmatrix} \dot{q}. \quad (13)$$

MW-AHRSv1 as IMU is used to measure the orientation of  $(\phi, \theta, \psi)$  and body angular velocity  $(\omega_x, \omega_y, \omega_z)$  of the cockpit and the data are acquired by XBee module at 100 Hz. The encoder with 10 000 resolution is used to measure

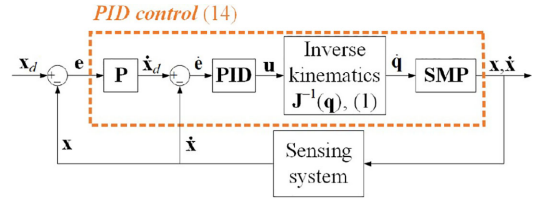


Fig. 4. PID control system for SMP.

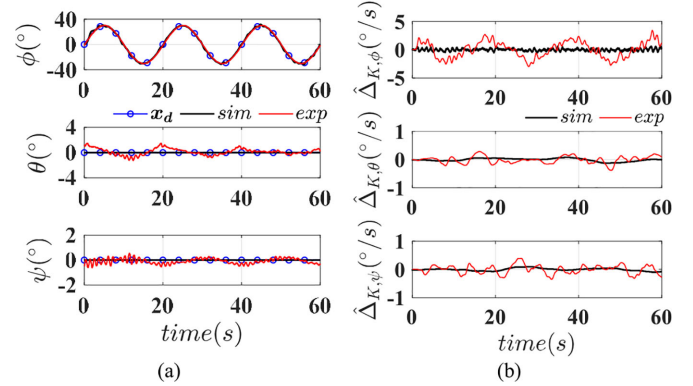


Fig. 5. Performance comparison of simulation and experimental results for DOB-SMC. (a) Tracking results. (b) Results of estimation of kinematic uncertainties.

the position of the linear stage accurately. Then, the position ( $P_0$ ) and the velocity ( $\dot{P}_0$ ) of the cockpit are computed from the encoder through a low-pass filter to minimize measurement noises. The filter is designed at 30 Hz of the cutoff frequency and implemented to IMU and encoder. NI crio-9082 with 533 MHz real-time processor and 256 MB of DDR2RAM drives the control algorithm at 50 Hz (0.02 s) with six control modules NI-9512. Fig. 3 shows the SMP with the cockpit sphere as a flight simulator with a flight scene projected from the projector and flight instrument and control panels.

#### A. Numerical Simulations

The tracking control is numerically simulated in the presence of uncertainties with PID, I-SMC, and DOB-SMC using (6), (14), and (16), respectively, shown in Figs. 5 and 6, and the results are compared to validate the performance against disturbances and uncertainties. First, the cascade PID control in Fig. 4 is designed as follows:

$$\begin{aligned} u &= k_{2,P}(k_{1,P}e - \dot{x}) + k_{2,I} \int (k_{1,P}e - \dot{x}) dt \\ &\quad + k_{2,D}(k_{1,P}\dot{e} - \ddot{x}) \\ &= k_{1,P}(k_{2,P}e + k_{2,I} \int e dt + k_{2,D}\dot{e}) \\ &\quad - (k_{2,I}\dot{x} + k_{2,P}\ddot{x} + k_{2,D}\ddot{x}) \end{aligned} \quad (14)$$

where  $k_{1,P}$  is a coefficient of outer P control;  $k_{2,P}$ ,  $k_{2,I}$ , and  $k_{2,D}$  are coefficients of inner P, I, and D control, respectively. The cascade PID controller removes the disturbances faster than

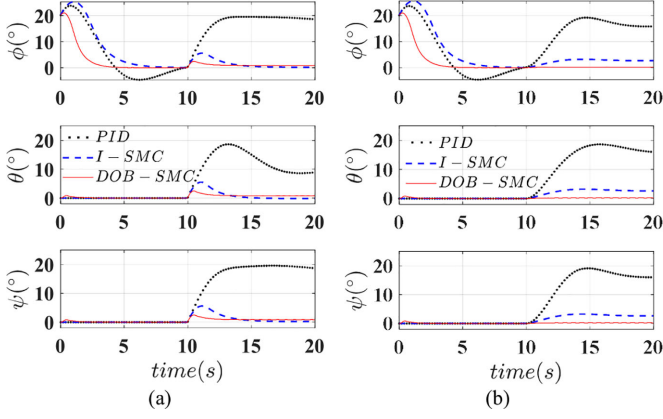


Fig. 6. Effects of constant uncertainties. (a) Kinematic uncertainties. (b) Dynamic uncertainties.

TABLE III  
LIST OF SPECIFICATIONS OF CONTROL PARAMETERS

DOB-SMC			
$\lambda_0$	3	$\lambda_1, \lambda_2$	1
$k_1^*$	2.8 (4)	$L_i$	10, $i=1,2,\dots,6$
$\rho_D$	3	$p^*$	19/23 (27/29)
$c_1$	3.2	$c_2^*$	9 (4)
I-SMC			
$c_1^*$	3.7 (3.2)	$\rho_D$	3
$c_2^*$	10 (6)		
PID controller			
$k_{1,p}^*$	1 (0.95)	$k_{2,p}^*$	1 (0.8)
$k_{2,f}^*$	0.001 (0.001)	$k_{2,d}^*$	0.006 (0.05)

\*gain parameters for position (orientation) control.

conventional PID control but still limited to handle numerous uncertainties.

For better performance, the I-SMC is applied to deal with the uncertainties. The sliding surface  $\sigma$  is defined as follows:

$$\sigma = \dot{\mathbf{e}} + c_1 \mathbf{e} + c_2 \int \mathbf{e} dt. \quad (15)$$

The corresponding control law is also designed as follows:

$$\mathbf{u} = \mathbf{f}(\mathbf{x}, \dot{\mathbf{x}}) + \mathbf{M}_A(\ddot{\mathbf{x}}_d + c_1 \dot{\mathbf{e}} + c_2 \mathbf{e}) + \frac{1}{2} \dot{\mathbf{M}}_A \sigma + \rho_D \text{sgn}(\sigma). \quad (16)$$

The stability of the I-SMC can be proved from  $V = \frac{1}{2} \sigma^T \mathbf{M}_A \sigma$ , (2), (15), and (16) as  $\dot{V} = -\sigma^T (\rho_D \text{sgn}(\sigma) - \Delta_D) = \|\sigma\|(\rho_D - b_D) \leq 0$ . The coefficients for each control method in Table III are determined from numerical simulations and then tuned by trial and error until good tracking performance is achieved.

**1) Comparison of Tracking Performance Between Simulations and Experiments for DOB-SMC:** The numerical simulations are demonstrated for orientation tracking control of the cockpit using MATLAB. The uncertainties are extracted from the actual experimental data to make the simulations become reliable. Moreover, the actuator limit is considered and detailed in Table II. The mechanical parameters for simulations are given in Table I. The control gains for each simulation are adjusted to maximize control performance. The desired trajectory is set as

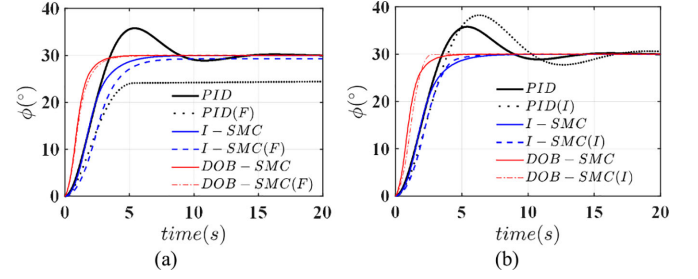


Fig. 7. Effects of parameter uncertainties. (a) Uncertain friction. (b) Uncertain inertia. (F) and (I) represent the presence of uncertain friction torque and inertia, respectively.

$[30\sin(0.1\pi t) \ 0 \ 0]^T$  along roll motion from zero initial condition ( $\phi_0 = \theta_0 = \psi_0 = 0^\circ$ ). For the control system, the kinematic uncertainties  $\Delta_K$  are estimated from the DOB in (3) and utilized for the DOB-SMC in (6) to reject  $\Delta_K$  as well as  $\Delta_D$  during actual operation. Fig. 5 shows the simulation results of tracking performance compared with the experiments. The DOB-SMC can estimate various uncertainties, and the tracking error in the finite-time is bounded within smaller than  $2^\circ$  in Fig. 5(a).

Moreover, DOB performance to estimate  $\Delta_K$  during the trajectory tracking is compared with both simulations and experiments. The estimation results are similar to each other, but the experiments in Fig. 5(b) are larger than the simulation since the SMP has a number of uncertainties such as distorted cockpit sphere, surface contact, and slipping, unlike the simulations. The results can show the feasibility of estimation and tracking performance of the DOB-SMC regardless of the presence of the uncertainties validating the kinematic and dynamic models.

## 2) Simulation for Robustness Validation of DOB-SMC:

The robustness of the DOB-SMC is shown with numerical simulations. The cockpit is initially set as  $[20^\circ \ 0 \ 0]^T$  with an angular velocity of  $[10^\circ/\text{s} \ 0 \ 0]^T$ . The uncertainties  $\Delta_K = [10 \ 10 \ 10]^T$   $^\circ/\text{s}$  and  $\Delta_D = [6 \ 6 \ 6]^T$   $\text{N}\cdot\text{m}$  are injected to each simulation after 10 s. Fig. 6(a) and (b) show the tracking performance of the DOB-SMC compared with the PID and I-SMC. The DOB-SMC tracks more accurately than both I-SMC and PID in the presence of kinematic and dynamic uncertainties.

Similarly, the effects of uncertain parameters such as frictional torque and inertia on dynamics are investigated. The frictional torque is varying to  $-3\text{sgn}(\dot{\phi}) \text{ N}\cdot\text{m}$  due to the changing of inertia  $\pm 10 \text{ kg}\cdot\text{m}^2$  for human on board. The step input of  $30^\circ$  is applied for roll motion with and without uncertainties. Fig. 7 shows the performance of the controllers. The frictional torque dramatically affects the control performance of both PID and I-SMC, but the DOB-SMC shows the robustness against the parameter uncertainties.

## B. Experiments for Orientation and Position Control

The experimental results for PID, I-SMC, and DOB-SMC are compared using two different inputs: step and sinusoidal inputs. The comparison demonstrates the tracking performance of the proposed control system. The gain parameters for each controller in orientation and position tracking control, as given

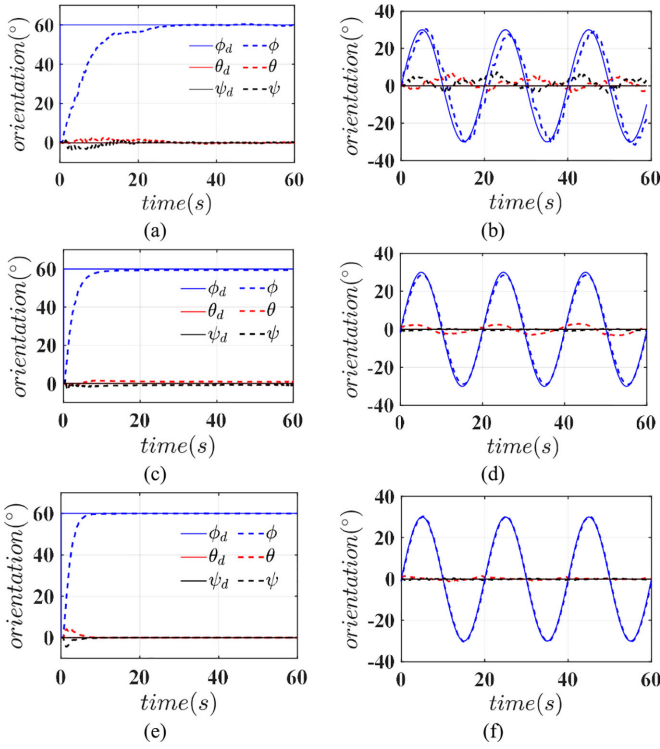


Fig. 8. Comparison of orientation tracking control results for step and sinusoidal inputs. (a), (b) PID. (c), (d) I-SMC. (e), (f) DOB-SMC.

TABLE IV  
COMPARISON OF ORIENTATION CONTROL PERFORMANCE FOR  
PID, I-SMC, AND DOB-SMC

Controller		$\phi$	$\theta$	$\psi$
Step Input	PID	0.22/0.53	0.19/0.56	0.21/0.73
	I-SMC	0.052/0.12	0.038/0.06	0.074/0.1
	DOB-SMC	0.026/0.051	0.015/0.04	0.072/0.09
Sinusoidal Input	PID	5.43/10.88	2.65/6.50	2.83/7.31
	I-SMC	1.46/2.86	1.94/3.35	0.40/0.86
	DOB-SMC	0.65/1.54	0.53/1.47	0.22/0.61

RMSE/ $e_{\text{Max}}$  (°).

in Table III, are determined by trial and error until good tracking performances are acquired from the basis of simulation results.

**1) Orientation Control:** Two inputs for tracking control of the cockpit are step and sinusoidal inputs;  $[\phi_d \theta_d \psi_d]^T = [60^\circ 0^\circ 0^\circ]^T$  and  $[30^\circ \sin(0.1\pi t) 0^\circ 0^\circ]^T$ , respectively. Initial orientation set as zero of  $\phi_0$ ,  $\theta_0$ , and  $\psi_0$ . The actual control input for each controller can be generated from (13). The tracking performance of three controllers is compared in Fig. 8. First, for the step response, the maximum error ( $e_{\text{Max}}$ ) of the DOB-SMC is  $0.09^\circ$  along all axes, but  $0.73^\circ$ , PID and  $0.12^\circ$ , I-SMC after 30 s. The root-mean-square error (RMSE) of the DOB-SMC, I-SMC, and PID after 30 s is  $0.072^\circ$ ,  $0.074^\circ$ , and  $0.22^\circ$ , respectively. The results are detailed in Table IV. Moreover, the error converges in finite time less than 10 s in the DOB-SMC compared with 30 s and 15 s in PID and I-SMC, respectively. The results show that the DOB-SMC has faster convergence and smaller steady-state error than PID and I-SMC in the presence of uncertainties.

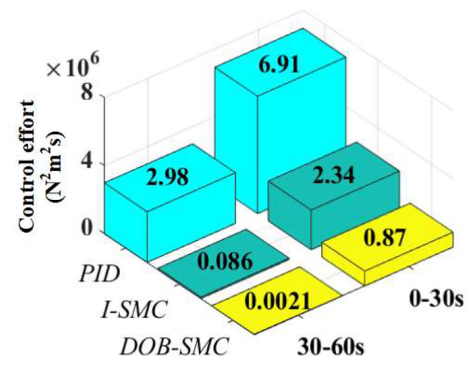


Fig. 9. Control efforts for PID, I-SMC, and DOB-SMC.

Next, the sinusoidal input is applied for 60 s.  $e_{\text{Max}}$  of the DOB-SMC is  $1.54^\circ$  along all axes, while  $10.88^\circ$  and  $3.35^\circ$  from PID and I-SMC, respectively, for 60 s. The RMSE of the DOB-SMC is  $0.65^\circ$  smaller than  $5.43^\circ$ , PID and  $1.94^\circ$ , I-SMC. The results indicate better orientation tracking performance. Moreover, computational time causes time delays between the input command and the output in the control loop. The DOB-SMC takes less than 0.1 s since it guarantees finite-time convergence in spite of uncertainties with smaller delays compared with PID ( $\approx 1$  s) and I-SMC ( $\approx 0.2$  s).

Control efforts defined as  $\sum_{i=1}^N (\|\mathbf{u}(i)\|^2 \Delta t(i))$  are computed where  $N$  is the number of total sampling steps in the experiments.  $\Delta t(i)$  is a time interval at the  $i$ th step. Fig. 9 shows the results from three controllers for the step response in Fig. 8(a), (c), and (e). The I-SMC and DOB-SMC need much smaller control efforts than PID. Besides, the DOB-SMC consumes the effort  $3\times$  and  $40\times$  smaller than I-SMC in both transient and steady states, respectively, since the uncertainties are effectively compensated and rejected from DOB estimation.

**2) Position Control:** The translational motion generated by the ball screw actuators has a mechanical limitation that is forward and reverse limit for safety. Then, the position of each actuator  $q_i$  must satisfy the following inequality,  $q_{\text{forward limit}} \leq q_i \leq q_{\text{reverse limit}}$ ,  $i = 1, 2, 3$ , where the limit position is detailed in Table I. The actuator input for each controller can also be generated from (13). When the cockpit moves along the translational axis within the motion range, rotation can occur due to kinematic coupling. Thus, six DOFs motion should be controlled. A desired command input is given as  $[(P_{0,x})_d (P_{0,y})_d (P_{0,z})_d]^T = [0.15\sin(0.04\pi t) 0.15\cos(0.04\pi t) 0]^T$  m and  $[\phi_d \theta_d \psi_d]^T = [0^\circ 0^\circ 0^\circ]^T$  with zero initial conditions for both position and orientation, respectively. Fig. 10 shows the comparison of position and orientation tracking control along the circular path with PID, I-SMC, and DOB-SMC. The  $e_{\text{Max}}$  in the DOB-SMC is  $0.008$  m along all axes, smaller than  $0.032$  m and  $0.01$  m in PID and I-SMC, respectively. The RMSE of the DOB-SMC is  $0.0056$  m smaller than  $0.023$  m, PID and  $0.0069$  m, I-SMC. Similarly, it is validated that the undesired coupled rotation during the translation is canceled out from the DOB-SMC. The  $e_{\text{Max}}$  is about  $1^\circ$  in the DOB-SMC smaller than  $4^\circ$  in PID and  $3^\circ$  in I-SMC in Fig. 10(e) and (f). The RMSE in the DOB-SMC is  $0.7^\circ$  smaller



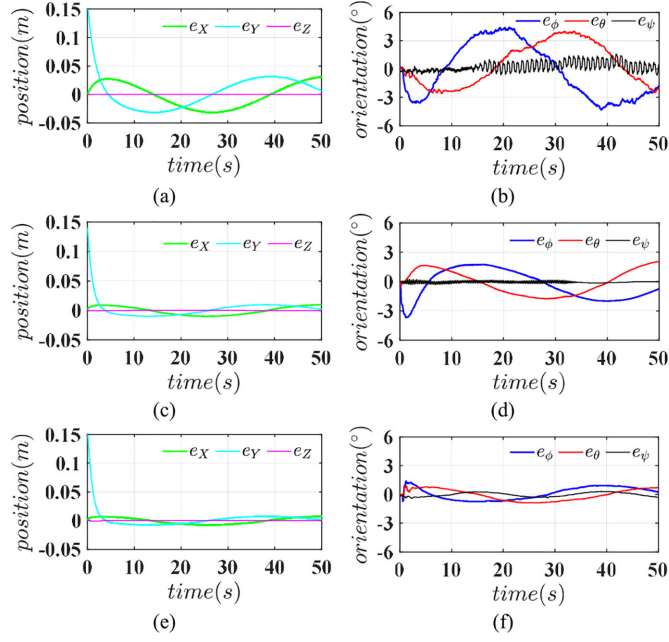


Fig. 10. Comparison of position and orientation tracking control results. (a), (b) PID. (c), (d) I-SMC. (e), (f) DOB-SMC.

TABLE V

COMPARISON OF POSITION AND ORIENTATION CONTROL PERFORMANCE FOR PID, I-SMC, AND DOB-SMC

position (m)	controller	X	Y	Z
	PID	2.1e-2/3.2e-2	2.3e-2/3.2e-2	5e-4/7e-4
coupled rotation (°)	I-SMC	6.9e-3/1.0e-2	1.6e-2/1.0e-2	3.2e-4/5e-4
	DOB-SMC	5.2e-3/8e-3	5.6e-3/8e-3	3e-4/5e-4
	controller	$\phi$	$\theta$	$\psi$
	PID	2.91/4.41	2.25/4.02	0.55/1.59
	I-SMC	1.53/3.67	1.22/2.04	0.11/0.31
	DOB-SMC	0.64/1.37	0.58/0.89	0.21/0.42

RMSE/ $e_{\text{Max}}$

than  $2.9^\circ$  and  $1.5^\circ$  in PID and I-SMC, respectively. The detailed results are summarized in Table V. The experimental results show that the orientation and position tracking performance of the DOB-SMC are better than the PID and I-SMC even in the presence of uncertainties similar to the numerical simulation.

### C. Experiments of Flight Maneuvers

Actual flight simulations are demonstrated using the SMP for VR. Two typical flight maneuvers are explored as phugoid and dutch roll modes related to lateral and longitudinal motion, respectively. The flight dynamics are utilized to obtain the trajectory based on the real flight to increase the reality detailed in [26]. The dynamic equations are solved from MATLAB to generate the trajectories for the SMP. The rotational motion is fully driven without any scaling and limiting from the advantages of the SMP with unlimited rotation. In contrast to translational motion, high-pass filters, as well as scaling and limiting, are used for the position trajectory due to the limitation of motion range.

**1) Phugoid Mode:** The phugoid mode is an oscillating motion along a longitudinal direction and pitch axis with a lightly

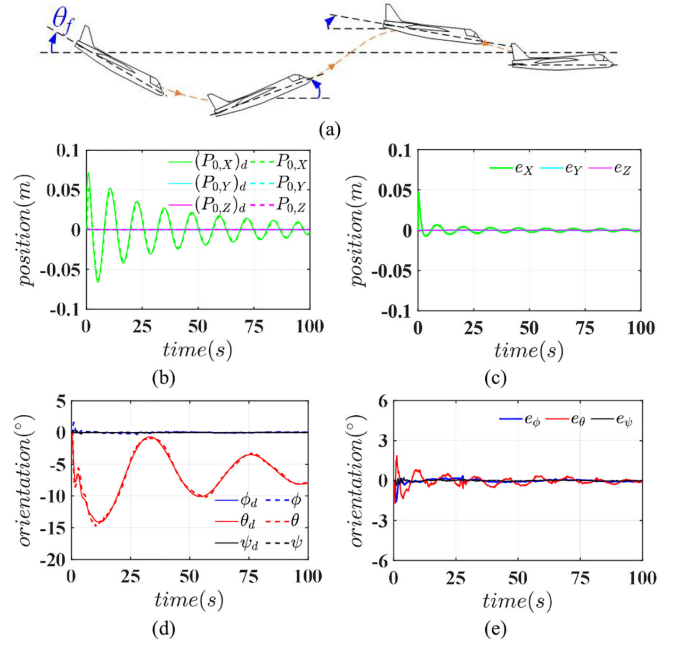


Fig. 11. Experimental results for phugoid mode. (a) Side view. (b), (c) – Tracking performance for position. (d), (e) – Tracking performance for orientation.

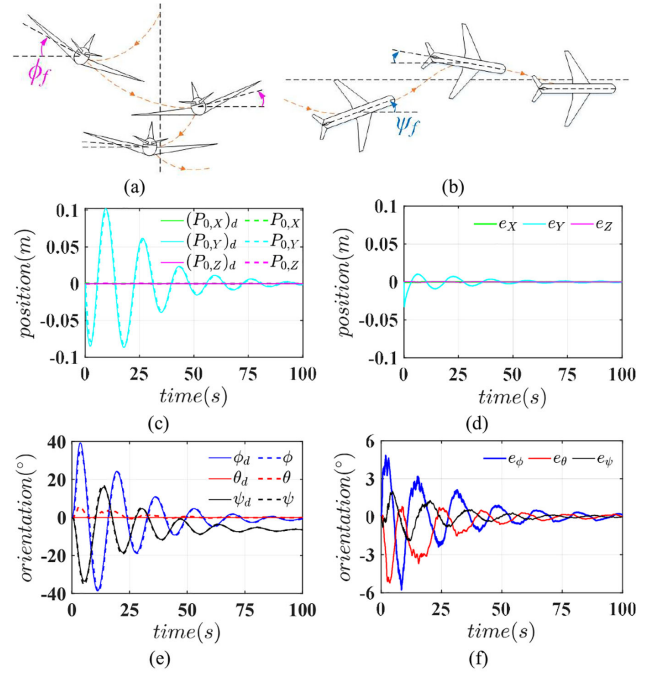


Fig. 12. Representation and experimental results for dutch roll mode. (a) Front view. (b) Top view. (c), (d) – Tracking performance for position. (e), (f) – Tracking performance for orientation.

damped low frequency, as shown in Fig. 11(a). Fig. 11(b)–(e) shows the tracking results for experiments of the phugoid motion, including position and orientation. The tracking performance is demonstrated from the results for the trajectory using DOB-SMC within  $1.3^\circ$  of  $e_{\text{Max}}$ .



**2) Dutch Roll Mode:** The dutch roll mode is one of the classical dynamic response of flight, which is a complex interaction between three lateral-directional DOFs motion composed of sideslip, rolling, and yawing. The oscillatory conversion between rolling and yawing occurs, as shown in Fig. 12(a) and (b). The Fig. 12(c)–(f) shows tracking results for experiments of the dutch roll mode coupled between three DOFs motion. The tracking performance is validated from the experimental results for the desired trajectory, applying proposed control within the  $e_{\text{Max}}$  of  $6^\circ$  initially. The error converges after 50 s within  $1^\circ$  in spite of highly coupled motion. The results show accurate tracking performance to simulate actual flight motion successfully, and the SMP and DOB-SMC can be applied to the flight simulator for VR applications.

## V. CONCLUSION

In this article, we presented the robust control system referred to as DOB-SMC of the SMP driven by spherical wheels capable of providing unlimited rotation along all axes for a flight simulator. The uncertain kinematics (distorted cockpit sphere, surface contact, slipping, etc.) was estimated from the DOB, and then the SMC was applied for dynamic uncertainties and disturbances (unknown inertia, gravity, friction, etc.). The finite-time convergence in the presence of the uncertainties was proved for the DOB-SMC. The results of numerical simulation demonstrated the tracking performance for the DOB-SMC compared with the PID control and I-SMC. The control gain for experiments was obtained from the analysis of simulations. The experimental results validated better position and orientation tracking performance of the DOB-SMC despite dynamic uncertainties as well as kinematic uncertainties compared with the PID control and I-SMC. Two flight maneuvers with phugoid and dutch roll mode were experimented using trajectories computed from flight dynamics to improve the sense of reality. The experimental results demonstrate that the SMP can be utilized as a flight simulator for VR. In particular, it can help a pilot training flight skills in emergency situations, such as a helicopter with a malfunction of the tail blade, aircraft recovery from a stall, etc.

## REFERENCES

- [1] H. Arioui, L. Nehaoua, S. Hima, N. Ségué, and S. Espié, "Mechatronics, design, and modeling of a motorcycle riding simulator," *IEEE/ASME Trans. Mechatron.*, vol. 15, no. 5, pp. 805–818, Oct. 2010.
- [2] L. Nehaoua, H. Arioui, and S. Mammar, "Motorcycle riding simulator: How to estimate robustly the rider's action," *IEEE Trans. Veh. Technol.*, vol. 62, no. 1, pp. 80–88, Jan. 2013.
- [3] L. Nehaoua, H. Mohellebi, A. Amouri, H. Arioui, S. Espié, and A. Kheddar, "Design and control of a small-clearance driving simulator," *IEEE Trans. Veh. Technol.*, vol. 57, no. 2, pp. 736–746, Mar. 2008.
- [4] H. Arioui, S. Hima, L. Nehaoua, R. J. V. Bertin, and S. Espié, "From design to experiments of a 2-DOF vehicle driving simulator," *IEEE Trans. Veh. Technol.*, vol. 60, no. 2, pp. 357–368, Feb. 2011.
- [5] M. Dagdelen, G. Reymond, A. Kemeny, M. Bordier, and N. Maïzi, "Model-based predictive motion cueing strategy for vehicle driving simulators," *Control. Eng. Pract.*, vol. 17, no. 9, pp. 995–1003, Sep. 2009.
- [6] A.-A. Samji and L. D. Reid, "The detection of low-amplitude yawing motion transients in a flight simulator," *IEEE Trans. Syst., Man, Cybern.*, vol. 22, no. 2, pp. 300–306, Mar./Apr. 1992.
- [7] S. K. Advani, M. A. Nahon, N. Haeck, and J. Albronda, "Optimization of six-degrees-of-freedom motion systems for flight simulators," *J. Aircraft*, vol. 36, no. 5, pp. 819–826, Sep./Oct. 1999.
- [8] P. Miermeister *et al.*, "The cablerobot simulator large scale motion platform based on cable robot technology," in *Proc. IEEE/RSJ Intell. Robots. Syst.*, Oct. 2016, pp. 3024–3029.
- [9] T. Miunske, J. Pradipta, and O. Sawodny, "Model predictive motion cueing algorithm for an overdetermined Stewart platform," *ASME J. Dyn. Syst., Meas., Control*, vol. 141, no. 2, Feb. 2019, Art. no. 021006.
- [10] M. Katliar, F. M. Drop, H. Teufel, M. Diehl, and H. H. Bühlhoff, "Real-time nonlinear model predictive control of a motion simulator based on a 8-DOF serial robot," in *Proc. Eur. Control Conf.*, Jun. 2018, pp. 1529–1535.
- [11] P. R. Kumar, A. K. Behera, and B. Bandyopadhyay, "Robust finite-time tracking of Stewart platform: A super-twisting like observer-based forward kinematics solution," *IEEE Trans. Ind. Electron.*, vol. 64, no. 5, pp. 3776–3785, May 2017.
- [12] D. Stewart, "A platform with 6 degrees of freedom," *Proc. Inst. Mech. Eng.*, vol. 180, pp. 371–386, 1965/1966.
- [13] H. Son and K.-M. Lee, "Open-loop controller design and dynamic characteristics of a spherical wheel motor," *IEEE Trans. Ind. Electron.*, vol. 57, no. 10, pp. 3475–3482, Oct. 2010.
- [14] K. Bai, R. Xu, K.-M. Lee, W. Dai, and Y. Huang, "Design and development of a spherical motor for conformal printing of curved electronics," *IEEE Trans. Ind. Electron.*, vol. 65, no. 11, pp. 9190–9200, Nov. 2018.
- [15] Z. Copeland, B. Jung, M. J. D. Hayes, and R. G. Langlois, "Full-scale atlas motion platform: Structures; actuation; control," *Int. J. Mech. Robot. Syst.*, vol. 3, no. 2/3, pp. 94–112, Dec. 2016.
- [16] S.-M. Lee and H. Son, "Multidegree-of-freedom motion platform based on spherical wheels," *IEEE/ASME Trans. Mechatronics*, vol. 22, no. 5, pp. 2121–2129, Oct. 2017.
- [17] S.-M. Lee and H. Son, "Improvement of design and motion control for motion platform based on spherical wheels," *IEEE/ASME Trans. Mechatronics*, vol. 24, no. 5, pp. 2427–2433, Oct. 2019.
- [18] K. Klumper, A. Morbi, K. J. Chisholm, R. Beranek, M. Ahmadi, and R. Langlois, "Orientation control of Atlas: A novel motion simulation platform," *Mechatronics*, vol. 22, pp. 1112–1123, 2012.
- [19] W.-H. Chen, D. J. Ballance, P. J. Gawthrop, and J. O'Reilly, "A nonlinear disturbance observer for robotic manipulators," *IEEE Trans. Ind. Electron.*, vol. 47, no. 4, pp. 932–938, Aug. 2000.
- [20] H. Liu, X. Tian, G. Wang, and T. Zhang, "Finite-time  $H_\infty$  control for high-precision tracking in robotic manipulators using backstepping control," *IEEE Trans. Ind. Electron.*, vol. 63, no. 9, pp. 5501–5513, Sep. 2016.
- [21] Q. Meng, T. Zhang, X. Gao, and J.-Y. Song, "Adaptive sliding mode fault-tolerant control of the uncertain Stewart platform based on offline multibody dynamics," *IEEE/ASME Trans. Mechatronics*, vol. 19, no. 3, pp. 882–894, Jun. 2014.
- [22] C.-H. Chiu and W.-R. Tsai, "Design and implementation of an omnidirectional spherical mobile platform," *IEEE Trans. Ind. Electron.*, vol. 62, no. 3, pp. 1619–1628, Mar. 2015.
- [23] J. Yang, S. Li, and X. Yu, "Sliding-mode control for systems with mismatched uncertainties via a disturbance observer," *IEEE Trans. Ind. Electron.*, vol. 60, no. 1, pp. 160–169, Jan. 2013.
- [24] A. Levant, "Higher-order sliding modes, differentiation and output-feedback control," *Int. J. Control*, vol. 76, no. 9/10, pp. 924–941, 2003.
- [25] S. Li and Y.-P. Tian, "Finite-time stability of cascade time-varying systems," *Int. J. Control*, vol. 80, no. 4, pp. 646–657, Apr. 2007.
- [26] M. V. Cook, *Flight Dynamics Principles: A Linear Systems Approach to Aircraft Stability and Control*. Oxford, U.K.: Elsevier, 2013.



**Seong-Min Lee** (Student Member, IEEE) received the B.S. degree in mechanical and nuclear engineering from the Ulsan National Institute of Science and Technology (UNIST), Ulsan, South Korea, in 2015. He is currently working toward the M.S. and Ph.D. joint degree with the school of Mechanical, Aerospace, and Nuclear Engineering, UNIST.

His research interests include mechanical system modeling, driving simulator, human-machine interaction, and control.



**Kewei Xia** received the Ph.D. degree in control theory and applications from Beihang University, Beijing, China, in 2017.

He was a Postdoctoral Fellow with Yonsei University Observatory, Yonsei University, Seoul, South Korea, from 2017 to 2018. He is currently a Postdoctoral Researcher with the School of Mechanical, Aerospace, and Nuclear Engineering, Ulsan National Institute of Science and Technology, Ulsan, South Korea. His current research interests include nonlinear control, spacecraft control, and unmanned aerial vehicle control.



**Hungsun Son** (Member, IEEE) received the M.S. degree in aero and astronautical engineering from Stanford University, Stanford, CA, USA, in 2002, and the Ph.D. degree in mechanical engineering from the Georgia Institute of Technology, Atlanta, GA, USA, in 2007.

He is currently an Associate Professor in Mechanical, Aerospace, and Nuclear Engineering, Ulsan National Institute of Science and Technology, Ulsan, South Korea. His current research interests include mechatronics, sensors and actuators, dynamic system modeling, design optimization, automation, and control.